https://dx.doi.org/10.1016/j.jmst.2021.10.034

In situ neutron diffraction unravels deformation mechanisms of a strong and ductile FeCrNi medium entropy alloy

L.Tang[a], F.Q.Jiang[b], J.S.Wróbel[c], B.Liu[d], S.Kabra[e], R.X.Duan[a], J.H.Luan[f], Z.B.Jiao[g], M.M.Attallah[a], D.Nguyen-Manh[h], B.Cai[a]

a School of Metallurgy and Materials, University of Birmingham, B15 2TT, United Kingdom

b Institute of Metal Research, Chinese Academy of Sciences, Shenyang 110016, China

c Faculty of Materials Science and Engineering, Warsaw University of Technology, ul. Wołoska 141, Warsaw 02-507, Poland

d State Key Laboratory for Powder Metallurgy, Central South University, Changsha 410083, China

e Rutherford Appleton Laboratory, ISIS Facility, Didcot OX11 0QX, United Kingdom

f Department of Materials Science and Engineering, City University of Hong Kong, Kowloon, Hong Kong, China

g Department of Mechanical Engineering, The Hong Kong Polytechnic University, Hung Hom, Hong Kong, China

h CCFE, United Kingdom Atomic Energy Authority, Abingdon, Oxfordshire OX14 3DB, United Kingdom

Abstract

We investigated the mechanical and microstructural responses of a high-strength equal-molar medium entropy FeCrNi alloy at 293 and 15 K by in situ neutron diffraction testing. At 293 K, the alloy had a very high yield strength of 651 ± 12 MPa, with a total elongation of 48% ± 5%. At 15 K, the yield strength increased to 1092 ± 22 MPa, but the total elongation dropped to 18% ± 1%. Via analyzing the neutron diffraction data, we determined the lattice strain evolution, single-crystal elastic constants, stacking fault probability, and estimated stacking fault energy of the alloy at both temperatures, which are the critical parameters to feed into and compare against our first-principles calculations and dislocation-based slip system modeling. The density functional theory calculations show that the alloy tends to form short-range order at room temperatures. However, atom probe tomography and atomic-resolution transmission electron microscopy did not clearly identify the short-range order. Additionally, at 293 K, experimental measured single-crystal elastic constants did not agree with those determined by first-principles calculations with short-range order but agreed well with the values from the calculation with the disordered configuration at 2000 K. This suggests that the alloy is at a metastable state resulted from the fabrication methods. In view of the high yield strength of the alloy, we calculated the strengthening contribution to the yield strength from grain boundaries, dislocations, and lattice distortion. The lattice distortion contribution was based on the Varenne-Luque-Curtine strengthening theory for multi-component alloys, which was found to be 316 MPa at 293 K and increased to 629 MPa at 15 K, making a significant contribution to the high yield strength. Regarding plastic deformation, dislocation movement and multiplication were found to be the dominant hardening mechanism at both temperatures, whereas twinning and phase transformation were not prevalent. This is mainly due to the high stacking fault energy of the alloy as estimated to be 63 mJ m−2 at 293 K and 47 mJ m−2 at 15 K. This work highlights the significance of lattice distortion and dislocations played in this alloy, providing insights into the design of new multi-component alloys with superb mechanical performance for cryogenic applications.

Keywords: Medium entropy alloy; Multi-component alloy; Cryogenic temperature; Neutron diffraction.

1. Introduction

In the past decade, a revolutionary new metallurgy design strategy, multi-component alloys (MCAs), containing several equimolar or non-equimolar components (in the range of 5 at.%−35 at.%), has been developed [1], which include high entropy alloys (HEAs) and medium entropy alloys (MEAs). Among different groups of MCAs, the group based on 3*d* transition elements (Cr, Mn, Fe, Co, Ni, V, and Cu) can form a single face-centered cubic (FCC) structure, which shows great potential in achieving superior strength–ductility combinations [2], [3], [4], [5], [6], [7], [8], [9]. The compositions include FeNiCo MEA [2], FeMnCoCr HEA [8], CrMnFeCoNi HEA [9], and other variations.

Recently, the intriguing mechanical performance of 3*d* element-metal MCAs under cryogenic temperatures has been demonstrated, such as high fracture tolerance [9], fatigue-crack growth resistance [10], and exceptional strength–ductility balance [11,12]. This makes them highly desirable in the rapid-growing cryogenic applications such as liquid gas storage, fusion reactors, and medical diagnosis. The application of MCAs at cryogenic temperatures, however, can be severely limited since the yield strength (YS) of those alloys is relatively low compared to conventional structural alloys. Many studies show that the YS of these MCAs is generally lower than 400 MPa at room temperature and 500 MPa at cryogenic temperatures [2,13]. For example, the YS of a single-phase FeCoCrNi HEA was only 260 MPa at 293 K and 480 MPa at 77 K [13]. Therefore, several conventional strengthening strategies (such as precipitating hardening and grain refinement) were applied to overcome this dilemma via introducing extensive dislocations and interfaces.

Based on the uniqueness of MCAs, two promising strengthening strategies are emerging to resolve this dilemma: chemical short-range order (SRO) [14], [15], [16] and severe lattice distortion (i.e., a wide fluctuation of the atomic bond distances) [1]. SRO stems from the enthalpic interactions among constituent elements, and its formation is thermodynamically favored in MCAs [14], [15], [16]. The densely distributed SROs can create strain fields, and thus, an extra force is required to break the SROs when dislocations pass by. The cutting-through and the following de-trapping process during dislocation migration are expected to increase the opportunity for dislocation to interact and form entanglement [15]. SROs have been observed in a VCoNi alloy [14] and a long-time-annealed CrCoNi alloy [16].

Severe lattice distortion originates from the randomly distributed constituent elements with varying atomic radii as no matrix or host element could be defined in MCAs [1]. Each atom in MCAs thus experiences different stress fields created by its interaction with a set of different neighboring atoms. The role of the severe lattice distortion in strengthening the MCAs is under debate. Wu et al. [17] suggested that the large lattice distortion fluctuation can only provide weak Labusch-type pinning effects on dislocation motions. However, research has shown that enhancing the lattice distortion by adding extra vanadium can induce a significant YS improvement in both FCC and body-centered cubic (BCC) HEAs [4]. The critical role of lattice distortion in strengthening was also confirmed by theoretical studies, which successfully predicted the YS of several MCAs using solute misfit volumes as the core parameter [18,19]. These theories also predicted the growing strengthening effect of lattice distortion with decreasing temperature [2].

Herein, we studied a new equimolar ternary MEA (FeCrNi alloy), which has been shown to achieve high YS (644 MPa) and good elongation (54%) at room temperature [20]. Several critical questions can be raised for this alloy: (i) Does SRO exist in the FeCrNi alloy, as observed in CrCoNi [15] and VCoNi MEAs [14]? Is SRO the main strengthening factor? (ii) To what degree the severe lattice distortion can strengthen the alloy and what is its strengthening contribution at cryogenic temperatures? In addition, the alloy should have high stacking fault energy (>50 mJ m^{-2}) according to Ref. [21]. Twinning and phase transformation should not be operative, but the alloy still has very good ductility, so what are the underpinning mechanisms for the alloy to have a balanced combination of strength and ductility? This study intends to provide insights into these questions.

2. Materials and methods

2.1. Materials

Powder metallurgy was used to produce the FeCrNi MEA with a nominal composition of $Fe_{33.3}Cr_{33.3}Ni_{33.3}$. Detailed procedures for the fabrication can be found in Ref. [20]. High purity (> 99.99%) Fe, Cr, and Ni raw materials were melted in an induction vacuum furnace. The melted liquid was dropped through a ceramic cube and atomized by high purity Ar with a pressure of 4 MPa. The formed powder, with an average diameter of 50 μm, was then capsulated in a steel cylinder chamber ($\Phi50 \times 150$ mm). After degassing and preheating to 1200 °C for 1 h, the sample was subjected to hot extrusion immediately with an extrusion ratio of 7:1 and a velocity of ~10 mm s^{-1}. The extruded bars were then cooled down to room temperature in the air. The actual chemical composition of the sample was measured to be $Fe_{33.7}Cr_{33.7}Ni_{32.5}$ (at.%) by inductively coupled plasma mass spectrometry (ICP-MS).

2.2. *In situ* neutron diffraction

In situ time of flight neutron diffraction measurements during tensile tests were carried out at the beamline of ENGIN-X at ISIS, spallation neutron source, the Rutherford Appleton Laboratory, UK. The schematic illustration of the TOF neutron diffractometers and strain scanner can be seen in our previous work [22]. Originally, a pulsed beam of neutrons with a wide energy range (incident beam) traveled through a 100 K liquid methane moderator, and its horizontal and vertical angular divergence was then modified by two pairs of motorized slits (4 mm × 4 mm). A vacuum chamber and a 50 kN hydraulic stress rig with a horizontal loading direction (LD) were mounted 45°

to the incident beam. Behind the collimators (4 mm wide), two diffraction detector banks (radial and axial) were centered on horizontal diffraction angles of ±90° to the incident beam to collect the diffraction signals from grain planes subjected to tensile and compressive load, respectively. Before the tests, instrument parameters (e.g., primary and secondary flight path distances) and instrumental peak broadening effects were determined by measuring a strain-free standard CeO_2 calibrant. Dog-bone tensile samples were mounted on the stress rig, then the high vacuum and low-temperature conditions were stabilized for half an hour before the test. Diffraction patterns were collected for 20 min intervals between each loading step, iterating until fracture. Stress-control and displacement-control were used at the elastic and plastic stages, respectively. The *in situ* neutron diffraction and tensile testing were repeated on two specimens for both temperatures. The data collected at the same condition were very similar, and thus, the reproducibility was confirmed and only one of the data was analyzed. Rietveld refinement and single peak fitting (with pseudo-Voigt function) were performed with the GSAS software, allowing the determination of lattice parameters, peak position, and full width at half maximum (FWHM) of the peaks. The lattice strain is defined as the change of inter-planar spacing with respect to its original inter-planar spacing. Its evolution can be calculated by Eq. (1) according to Ref. [3]:(1)$\varepsilon hkl=dhkl-dhkl0dhkl0$where εhkl is the lattice strain of {*hkl*} grain family, $dhkl$ and $dhkl0$ are corresponding lattice spacings at the current stress state and stress-free state, respectively. Procedures for single crystal constant and dislocation density calculations were included in the Supplementary Materials.

2.3. First principal calculation

Density Functional Theory (DFT) for elastic constant calculations was performed within the Vienna Ab-initio Simulation Package (VASP) using the Projector Augmented Wave (PAW) method and spin-polarized electronic structure scheme [23, 24]. The electron exchange-correlation functional was in the Generalized Gradient Approximation (GGA) treated with Perdew-Burke-Ernzerhof parametrization [25]. All the calculations in this work were carried out within the PAW potentials for Cr, Fe, and Ni without semi-core electrons with the core configurations [Ar] 3d^{4}s^1, [Ar] 3d^{7}s^{1,} and [Ar] 3d^{9}s^1, respectively. The plane wave cut-off energy for the most of calculations was 400 eV. The total energy was converged to 10^{-6} eV cell^{-1} and the force components were relaxed to 10^{-3} eV $Å^{-1}$. Total energies used for elastic constant calculations were performed using the Monkhorst-Pack meshes [26] with 4 × 4 × 4 k-point for both 3 × 3 × 3 FCC-supercell configurations with 108 atoms per unit cell configurations and additional calculations with the 6 × 6 × 6 k-point meshes were also performed for checking the convergence. A more detailed description of elastic constants from first-principles DFT calculations in different intermetallic phases can be found in Refs. [27], [28], [29], [30], [31], [32].

For disordered alloys, conventional approaches for evaluating elastic constants from DFT techniques are usually based on so-called Coherent Potential Approximation (CPA) from which a single site mean-field theory is applied to treat completely random configurations with different chemical compositions. The CPA method has been employed to investigate elastic property maps from DFT calculations for the case of concentrated random FCC Fe-Cr-Ni alloys which are the main base for austenitic stainless steels [33, 34]. In the present study, an alternative DFT approach was employed to study the elastic properties of the FeCrNi medium-range entropy alloys. It was based on our recent and systematic work on the phase stability of both FCC and BCC Fe-Cr-Ni magnetic alloys using a combination of first-principles constructed Cluster Expansion (CE) Hamiltonian with exchange Monte Carlo simulations at a finite temperature [35].

The new approach allows us to investigate not only the free energy but also the disorder-order transition of alloys as a function of composition and temperature in terms of Warren–Colley [36, 37] SRO effects between different pairs of atoms. The theoretical expression of SRO parameters has recently been derived for MCAs in a matrix formulation [38], [39], [40], [41]. The chemical SRO parameter αnA,B between two species A and B for the *n*-th nearest neighbor shell can be defined as follows Eq. (2):(2)αnA,B=1−ynA,BxAxBwhere ynA,B denotes the pair probability, xA and xB are the concentration of A and B atoms, respectively. Segregation between A and B components gives rise to positive αnA,B, whereas the negative value of αnA,B means that there is a chemical ordering between them. When αnA,B=0, A and B atoms are found to be randomly distributed in alloys. Fig. 1(a, b) shows the atomistic configurations of medium-range and equiatomic FeCrNi alloys obtained from the present Monte Carlo simulations of the 9 × 9 × 9 FCC supercell for the two temperatures: 300 and 2000 K (Fig. 1(a, b)), respectively.

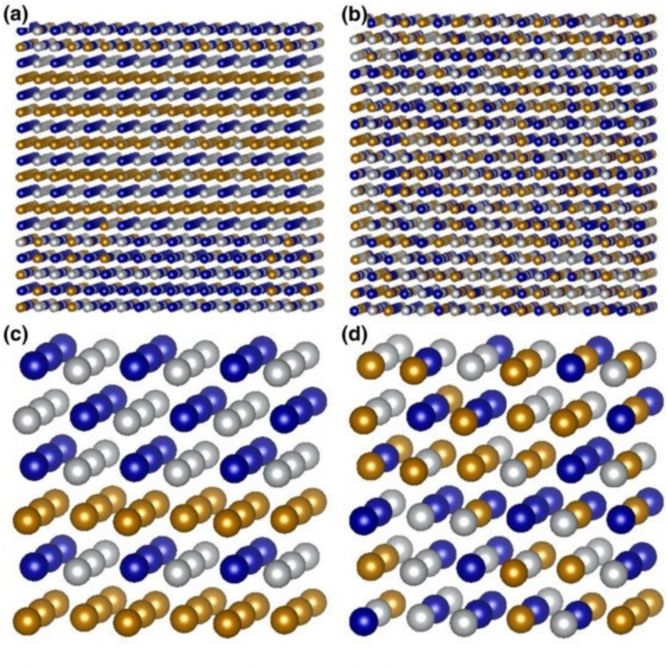

Fig. 1. Monte Carlo simulations of FCC supercell configurations for equiatomic FeCrNi alloys with different sizes and temperatures using DFT based CE Hamiltonian: (a) 9 × 9 × 9, 300 K; (b) 9 × 9 × 9, 2000 K; (c) 3 × 3 × 3, 300 K; (d) 3 × 3 × 3, 2000 K. The color code for Fe, Cr, and Ni is orange, blue and grey, respectively.

For the practical study of elastic constants in the FeCrNi system from first-principles methods, it is more convenient to reduce the supercell size from 9 × 9 × 9 (Fig. 1(a, b)) to 3 × 3 × 3 (Fig. 1(c, d)) to balance the computational time and accuracy of DFT calculations. Furthermore, for the high-temperature disordered configurations, the symmetry of the supercell is very low (space group $P1$) due to the random distribution of atoms in the supercell. Here, to obtain the individual components of the elastic constants matrix, we applied the method based on the deformation of an unstrained structure and the analysis of the changes in the total energy, E_{tot}, computed using DFT as a function of strain [42], [43], [44], [45]. The deformation leads to a change in the total energy of the crystal according to the following expressions Eq. (3):(3)U=Etot−E0V0=12∑i=16∑j=16cijεiεjwhere E_0 is the total energy of the unstrained lattice, V_0 is the volume of the undistorted cell and the C_{ij} is the elements of the elastic constant matrix with a notation that follows standard convention. Both i and j run from 1 to 6 in the sequence $\{xx, yy, zz, yz, xz, xy\}$. For each considered deformation, eight magnitudes of strain (±0.2%, ±0.4%, ±0.6%, ±0.8%) were applied. The dependencies of the total energy on the deformation were then fitted to quadratic equations and the respective elastic constants were obtained.

To study the elastic properties of Fe-Cr-Ni alloys at high-temperature configuration ($T = 2000$ K), strains were applied for nine different deformation modes:ε1={xx,0,0,0,0,0},ε2={0,yy,0,0,0,0}ε3={0,0,zz,0,0,0}ε4={xx,yy,0,0,0,0}ε5={xx,0,zz,0,0,0}ε6={0,yy,zz,0,0,0}ε7={0,0,0,yz,0,0}ε8={0,0,0,0,xz,0}ε9={0,0,0,0,0,xy}. This allowed obtaining nine elements of the elastic constant matrix (Eq. (4)):(4)(Cij)=[C11C12C13000C12C22C23000C13C23C33000000C44000000C55000000C66] Note: In this study, we assumed that the elements of the elastic constant matrix other than C_{11}, C_{12}, C_{13}, C_{22}, C_{23}, C_{33}, C_{44}, C_{55}, and C_{66} are equal to zero. Based on our previous study of structures with low symmetry [45], the values of those elements are usually much smaller than C_{11}, C_{12}, C_{13}, C_{22}, C_{23}, C_{33}, C_{44}, C_{55}, and C_{66} and can therefore be neglected. Therefore, the lack of those constants should not significantly influence the predictions of the overall elastic properties of alloys. For the low-temperature configuration ($T = 300$ K), the elastic tensor matrix elements have been computed by direct diagonalization following the tetragonal symmetry which will be discussed in the modeling section.

Afterward, we applied the calculation method of the anisotropy of Young's modulus and Poisson's ratio proposed by Wróbel et al. [32] to investigate the anisotropy of elastic properties. To obtain the theoretical values of elastic moduli for polycrystalline materials, the Reuss-Voigt-Hill method has been employed [46]. The detailed procedure can be found in Section 4 in the Supplementary Materials.

2.4. Microstructure characterization

The microstructure characterizations were performed on the samples sectioned from the fractured tensile bars using electrical discharge machining. The samples were metallographically polished before electron backscatter diffraction (EBSD) test on an HKL EBSD detector based on a scanning electron microscope (SEM, TESCAN MIRA 3, Czech Republic). The SEM parameters for the EBSD were set to a voltage of 20 kV, a current of 25 nA, and a step size of 1.5 μm. The EBSD data analysis was carried out with HKL Channel 5 software. To avoid ambiguous grain boundaries, misorientation angles less than 2° were ignored during the analysis. The thin foils for scanning transmission electron microscope (STEM) observation were mechanically polished to a thickness of ~80 μm before the twin-jet electropolishing using a constant current of 150 mA in a solution of 5% perchloric acid and 95% methanol cooled to –30 °C. The bright-field TEM observation was undertaken on a Tecnai G^2 F30 microscope operated at 300 kV. The atomic-resolution high-angle annular dark-field STEM (HAADF-STEM) images were performed on an aberration-corrected Titan 60–300 microscope at a voltage of 300 kV. The collection half-angles of the HAADF detector ranging from 60 to 290 mrad were used, with the convergence half-angle of 21.4 mrad, giving a probe size of ~1.2 Å. The dilatation field of the lattice was analyzed with the geometric phase analysis (GPA) method on the software Strain++ [47], during which a dislocation-free region was chosen as a reference.

Needle-shaped samples for atomic probe tomography (APT) were prepared by lift-out and annular milled in an FEI Scios focused ion beam (FIB)/SEM. The APT characterizations were performed in a local electrode atom probe (CAMEACA LEAP 5000 XR). The specimens were analyzed at 70 K in voltage mode, at a pulse repetition rate of 200 kHz, a pulse fraction of 20%, and an evaporation detection rate of 0.3% atom per pulse. The 3D reconstructions and data analysis were performed on Imago Visualization and Analysis Software (IVAS) version 3.8.

3. Experimental results

In this section, we first presented the microstructure and mechanical performance of the alloy at 293 and 15 K. We then presented the analysis of the *in situ* neutron diffraction spectra including the lattice strain, single-crystal elastic constants, the evolution of stacking fault probability (SFP), and dislocation density. Post-mortem TEM characterization was presented afterward.

3.1. Initial microstructure

Fig. 2 shows the micro to nanoscale microstructure of the virgin FeNiCr alloy characterized by SEM-based backscattered electrons (BSE), energy disperse X-ray analysis (EDS), EBSD, HRTEM, and APT. According to the EBSD inverse pole figure (IPF) map on the plane perpendicular to the loading direction (Fig. 2(a)), the alloy is composed of large equiaxed grains with annealing twins. The average grain size of ~23.4 μm was determined by performing the line-intercept method on the EBSD maps excluding the annealing twin boundaries. In Fig. 2(b), the band contrast map is overlapped with the boundaries map of Fig. 2(a). The low-angle grain boundaries (LAGBs) were defined as misorientations with $15° \geq \theta \geq 2°$ (shown in red lines) while the high-angle grain boundaries (HAGBs) comprised misorientations larger than 15° (shown in black lines). The annealing twin boundaries (TBs) were defined as $\Sigma3 = 60\ °\{111\}$ (shown in blue lines). The fraction of LAGBs was very low (less than 2%) and most of the boundaries were HAGBs. In addition to grain boundaries, a large fraction of annealing TBs was observed. SEM-BSE and corresponding EDS analysis results (Fig. 2(c)) show a small amount of Cr-rich phase located at grain boundaries. Typical bright-field TEM images of the annealing twin structure are shown in Fig. 2(d). Two straight and parallel twin boundaries can be identified with a spacing distance of

~2.18 µm. The twin relationship was confirmed by the corresponding selected area electron diffraction (SAED) pattern inserted in Fig. 2(d).

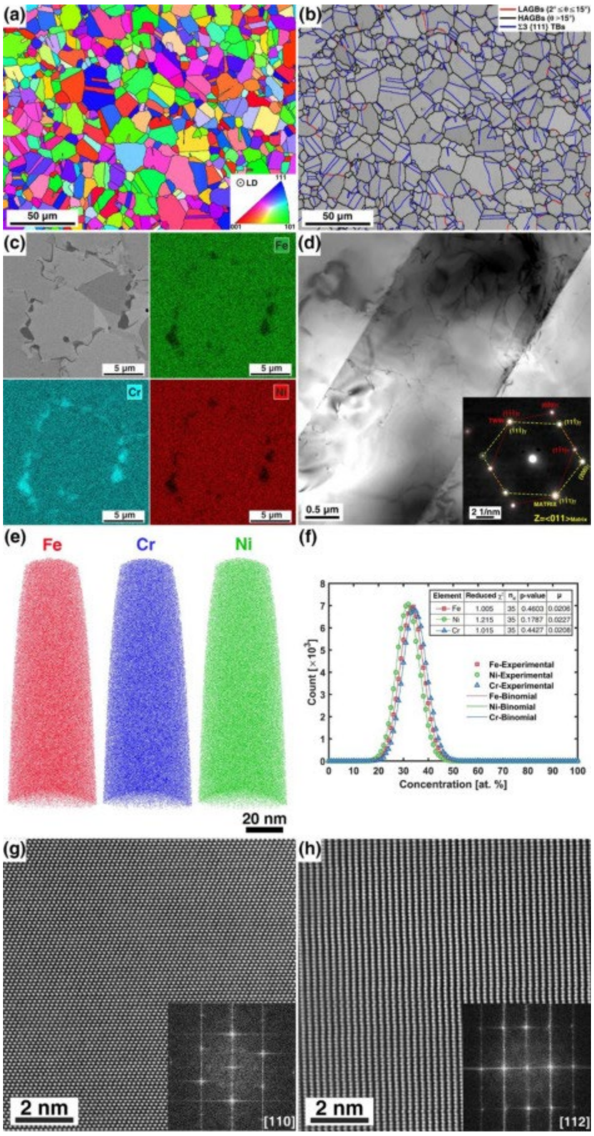

Element	Reduced χ^2	n_b	p-value	μ
Fe	1.005	35	0.4603	0.0206
Ni	1.215	35	0.1787	0.0227
Cr	1.015	35	0.4427	0.0208

Fig. 2. Microstructure characterization of the virgin FeCrNi sample: (a) EBSD map (inverse pole figure) perpendicular to loading direction (LD); (b) band contrast map overlapped with boundaries map of (a), the red, black, and green lines in the boundary map represent the low-angle grain boundaries (LAGBs), high-angle grain boundaries (HAGBs), and annealing twin boundaries (TBs, Σ3 {111}), respectively; (c) SEM-BSE images and corresponding elemental mapping of Fe, Cr, and Ni obtained from EDS; (d) typical bright TEM image and SAED pattern taken along [110] zone axes; (e) three-dimension APT tip reconstructions of Fe, Cr, and Ni atoms; (f) frequency distribution analysis of the three constituent elements and corresponding parameters used for qualifying the fit; (g) and (h) HRSTEM images and the corresponding FFT images of the alloy taken from [110] and [112] zone axis, respectively.

The chemical homogeneity of the alloy matrix was confirmed by APT analysis at the atomic scale. Fig. 2(e) displays the three-dimensional elemental maps of the three constituent elements, Fe, Cr, and Ni, from a reconstructed volume of

50 nm × 50 nm × 140 nm containing ∼12 million ions. There is no apparent elemental segregation in the tested volume. The tested region was found to have a composition of Fe 34.7, Ni 31.8, and Cr 33.5 (at.%), showing an acceptable match to the bulk composition obtained from the ICP-MS. Furthermore, the homogeneity of the atomic distribution of the alloy was also evaluated with the chi-squared statistics with a frequency distribution analysis (FDA) shown in Fig. 2(f). The curves from the binomial simulation match well with the curves obtained from the experiments, indicating a randomly distributed solid solution. The parameters used for qualifying the fit are shown in the insert table in Fig. 2(f). The normalized homogenization parameter, μ, for all three constituent elements was very close to 0, confirming their random distribution. As reported in Refs. [15,16], the existence of SROs can be confirmed by the diffuse superlattice features in the HRTEM images and the streaking intensity along the reciprocal lattice vectors in corresponding fast fourier transform (FFT) images. Therefore, to determine if SROs exist in the present alloy, we took over 20 HRSTEM images along different zone axes on the undeformed sample. Two of them are shown in Fig. 2(g, h), the inset images are the corresponding two-dimensional fast Fourier transforms (FFT) of the HRTEM images. Very vague diffusion disks were observed only in one of the HRTEM images (Fig. 2(h)), which may indicate the formation of a trace amount of SRO in the present alloy.

3.2. Tensile properties

Fig. 3(a) shows the engineering and true stress–strain curves (up to the UTS points) of the FeCrNi alloy at 293 and 15 K. The alloy shows a high YS of 651 ± 12 MPa and UTS of 1020 ± 3 MPa, as well as a great elongation of 48 ± 5% at 293 K. The mechanical properties of the alloy, were then compared with other high strength steels and single or multiphase MEAs/HEAs, as shown in Fig. 3(b), in which the YS was plotted versus total elongation [2,3,8,10,[48], [49], [50], [51], [52], [53],54,55]. The FeCrNi alloy shows an advantage in achieving high YS and a large elongation combination compared to other MCAs at 293 K.

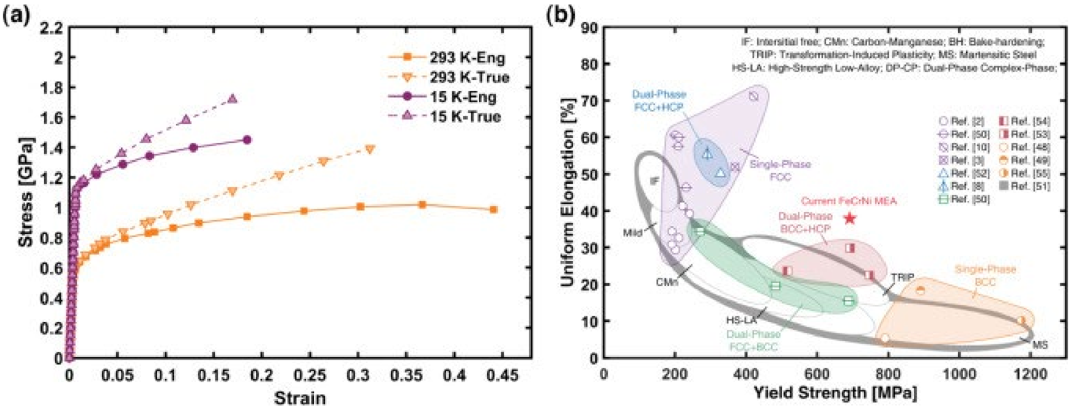

Fig. 3. (a) Engineering and true stress–strain curves of the alloy deformed at 293 and 15 K; (b) yield strength-uniform elongation comparison among the current FeCrNi MEA, several high-strength steels, and single or multi-phase MEAs/HEAs [2,3,8,10,[48], [49], [50], [51], [52], [53], [54], [55]].

At 15 K, the YS of the FeCrNi alloy increased to 1092 ± 27 MPa, the UTS increased to 1451 ± 2 MPa, while the total elongation decreased to 18% ± 1%. Corresponding values of strength and ductility are listed in Table 1. We have also listed the mechanical properties of several HEA/MEA and FCC alloys at 15 K or lower temperature in Table 1. The YS of FeCrNi alloy is highest among the listed alloys, although its elongation is much lower.

3.3. Neutron diffraction spectra

The *in situ* neutron diffraction patterns during tensile testing at 293 and 15 K plotted with respect to true stress were shown in Fig. 4(a, b), respectively. Five reflections of {111}, {200}, {220}, {311}, and {222} from the single FCC phase can be observed at both 293 and 15 K before deformation. During and after the tensile testing at both temperatures, no new peaks appeared, indicating the FCC structure was stable and maintained as a single FCC phase solid solution under loading. The lattice parameter (a_0) was obtained by performing Rietveld refinement on neutron diffraction patterns. The lattice parameter decreased slightly from 3.602 to 3.594 Å as the temperature decreased from 293 to 15 K due to the shrinkage of atomic bands [22].

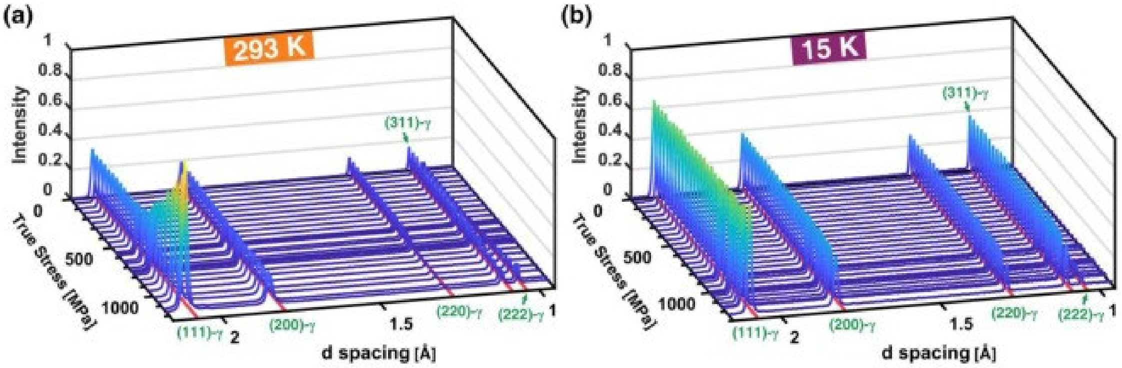

Fig. 4. *In situ* neutron diffraction spectra collected during deforming at (a) 293 K and (b) 15 K.

The measured lattice strain from five crystallographic planes of ({111}, {200}, {220}, {311}, and {222}) along axial and radial direction was plotted as a function of true stress in Fig. 5(a) and (b) (293 and 15 K). The uncertainties in the measured internal strains were approximately 30 microstrains. The measured bulk elastic Young's modulus (E_M) at different temperatures was obtained by linear fitting the true stress and strain curves at the elastic stage. Similarly, the elastic constants of each orientation (E111, E200, E220, and E311) were then obtained by linear fitting the lattice strain and true stress before yielding (Table 2). After yielding, the orientation-dependent yielding behaviors were observed at both temperatures. As indicated in Fig. 5(a, b) and Table 2, the {111} grain family has the highest stiffness (E111 of 248.1 GPa at 293 K and 260.4 GPa at 15 K). It, however, showed the earliest yielding behavior (~550 MPa at 293 K and ~1000 MPa at 15 K). Meanwhile, among all four grain families, {200} showed the lowest stiffness (E200 of 148.6 GPa at 293 K and 162.3 GPa at 15 K) and a delayed yielding behavior (~730 MPa at 293 K and ~1150 MPa at 15 K). The varied stiffness and yielding behaviors among different grain families can be ascribed to the elastic and plastic anisotropy of the crystals. After the yielding of some stiff grain families (e.g., {111}), the external stress gradually transferred to other soft grain families (e.g., {200}).

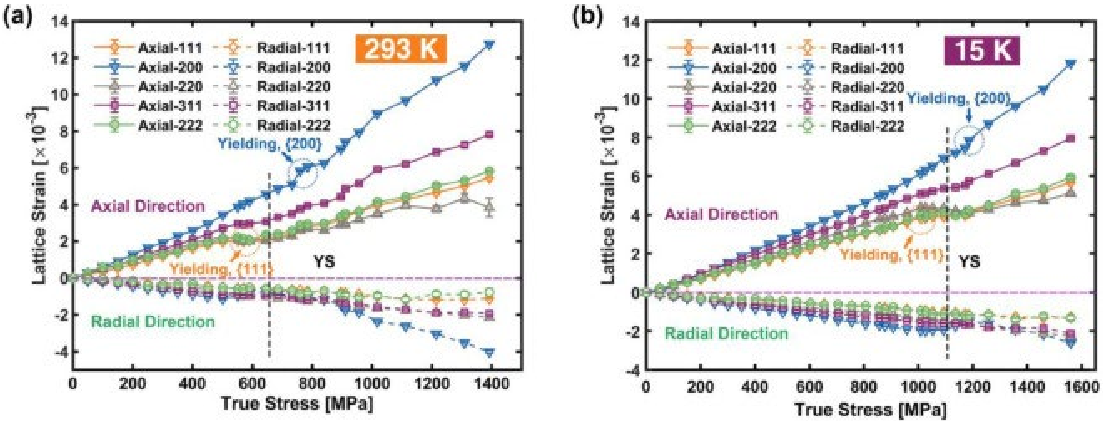

Fig. 5. Lattice strain evolution of crystallographic planes of {111}, {200}, {220}, {311}, and {222} from axial and radial directions during deforming at (a) 293 K and (b) 15 K.

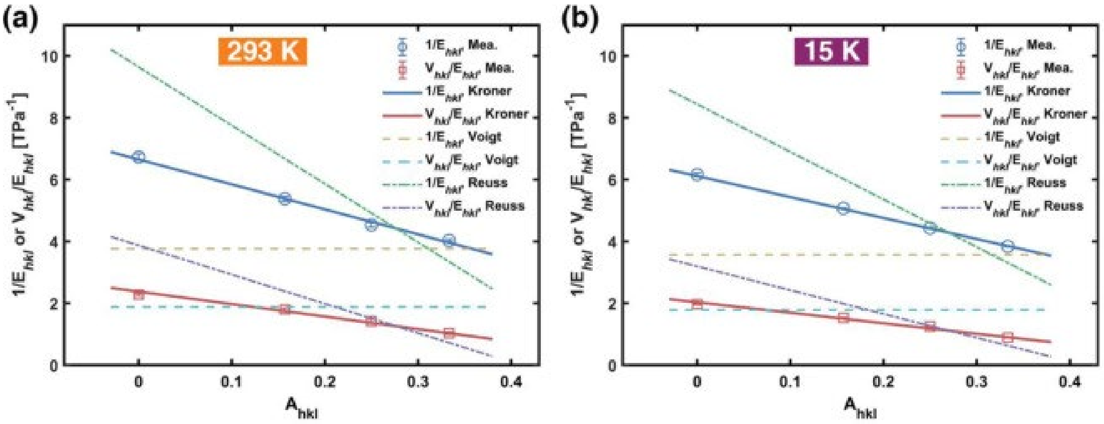

Fig. 6. The reciprocal diffraction elastic moduli ($1/E_{hkl}$ and v_{hkl}/E_{hkl}) plotted as a function of the elastic anisotropy factor, A_{hkl}, which were obtained from the experimental measured (Mea.) elastic lattice strain and fitted by Kroner, Voigt, and Reuss models at (a) 293 K and (b) 15 K, respectively.

3.4. Single-crystal elastic constants calculation

During elastic deformation, the lattice parameter obtained at axial and radial directions increased linearly with true stress. Their slopes at radial and axial directions were obtained by linear fitting and the ratio of the two slopes determines the Poisson's ratio (*v*). Then the shear modulus (*G*) was obtained via G=E/2(1+v). The drop of deformation temperature increased the stiffness of the alloy as the Ehklat all four orientations increased to varying degrees.

To better understand the underlying elastic deformation behavior of the alloy at different temperatures, several materials properties, including macroscopic elastic, shear, and bulk moduli (E_M, G_M, and K_M), were calculated from diffraction elastic moduli (E_{hkl}) and Poisson's ratio (v_{hkl}) using the Voigt, Reuss, and Kroner models [58]. The detailed procedure can be found in Section 1 of the Supplementary Materials.

In Fig. 6(a, b), the two reciprocal diffraction elastic constants ($1/E_{hkl}$and v_{hkl}/E_{hkl}) obtained from experimental elastic lattice strain and calculated with Voigt, Reuss, and Kroner models are plotted with respect to the elastic anisotropy factor $A_{hkl}=(h2k^2+h^2l^2+k^2l^2)/(h2+k^2+l^2)$ at 293 and 15 K, respectively. The fitting results indicate that among all three models, the Kroner model shows the best agreement with the experimental results at both 293 and 15 K. The Voigt model simply assumes that all grains are uniformly strained, but the force among grains cannot meet the equilibrium. While in the Reuss model, homogeneous stress is assumed to be applied to all grains, but the distorted grains cannot fit together. Therefore, due to their simplicity, the Voigt and Reuss model are generally used to define the upper and lower bounds of the diffraction and isotropic macroscopic elastic constants. By contrast, the Kroner model provides a more accurate estimation of elastic properties after considering the orientation dependence of elastic parameters. The single-crystal elastic constants, elastic, polycrystalline moduli, and Poisson’s ratio at 293 and 15 K calculated by this method are listed in Table 3. The values of C_{11} and C_{44} decreased slightly as the temperature decreased from 293 to 15 K, while C_{12} remains nearly constant.

The orientation-dependent elastic properties of the FeNiCr alloy at 293 K (determined from neutron diffraction and DFT simulation results) were illustrated in Fig. 7. To calculate the elastic properties in any direction, the fourth-order elastic tensor was transformed in a new basis with Eq. (S20) in the Supplementary Materials. The experimentally determined elastic properties of the alloy were illustrated with the three-dimensional (3D) surfaces (left column). The experimental results along directions at *XY, XZ*, and *YZ* planes were shown in the middle column by 2D contours. Young's modulus is shown in Fig. 7(a, e). The maximum and minimum values of 302 and 119 GPa were observed at 〈111〉 and 〈100〉 direction, respectively. The ratio of maximum-to-minimum elastic modulus of 2.5 indicates the high anisotropy property of the alloy. Shear modulus and Poisson's ratio were shown in Fig. 7(b, f), respectively. The translucent outer surface represents the maximum value while the solid surface inside shows the minimum values. The maximum and minimum values were shown with dashed and solid lines in the corresponding 2D contours. The maximum value of the shear modulus (127 GPa) appeared at 〈100〉 direction whereas the minimum value of 55.3 GPa is in 〈110〉 direction, yielding the ratio of the maximum to the minimum shear modulus of 2.3 (Fig. 7(c, g)). For Poisson's ratio, the maximum value is 0.4 (<100> direction) while the minimum value is approaching 0 (Fig. 7(c, g)). In Fig. 7(d, h), the linear compressibility (LC) has a value of 1.9 TPa^{-1}, showing negligible anisotropy in all directions.

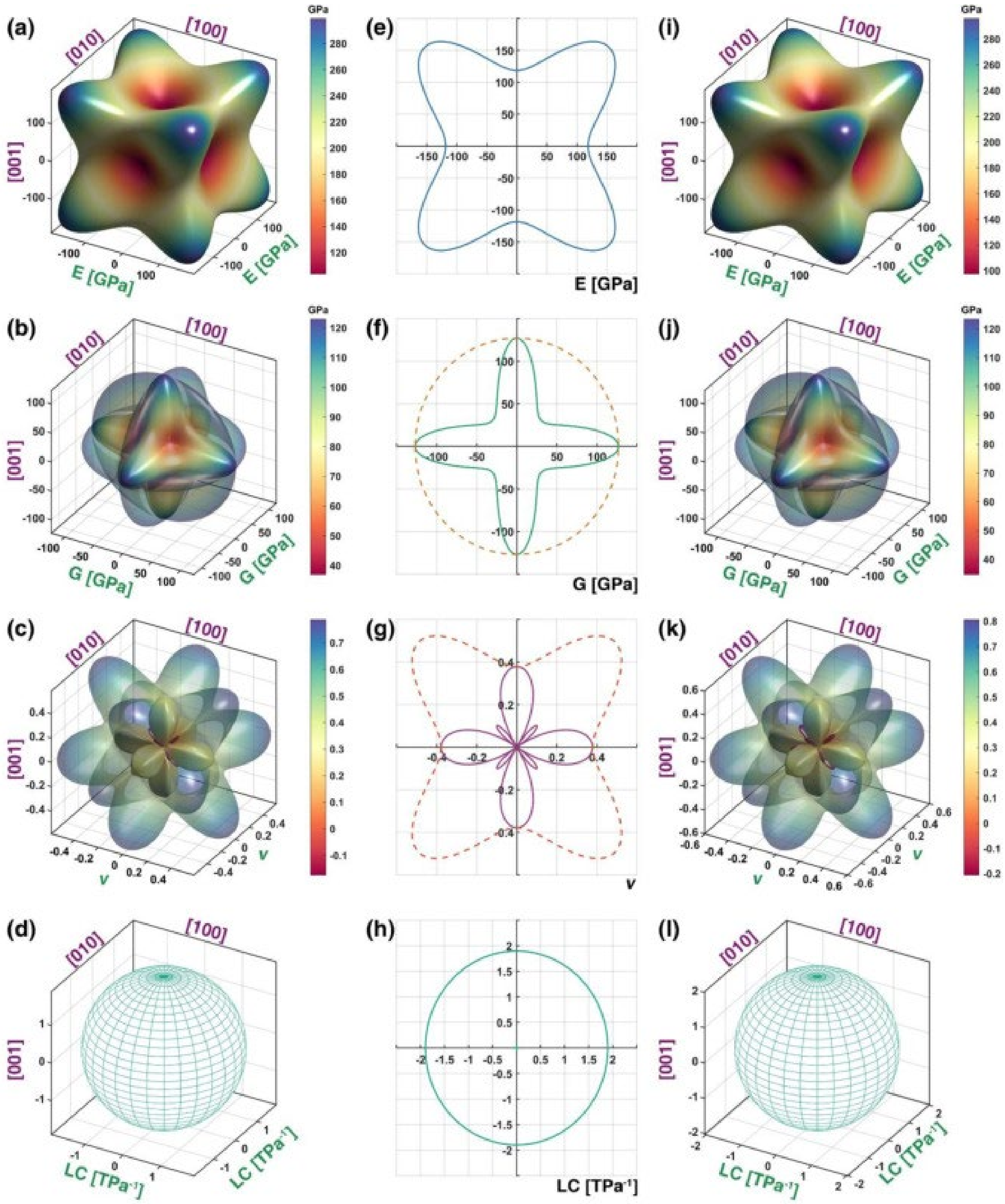

Fig. 7. Elastic properties of the FeNiCr alloy at 293 K determined via *in situ* neutron diffraction measurements (a–h) and DFT calculations (i–l). The magnitude concerning the directions in three dimensions for (a) and (i) Young's modulus, (b) and (j) shear modulus, (c) and (k) Poisson's ratio, and (d) and (l) linear compressibility. The maximum and minimum values of shear modulus and Poisson's ratio are represented by two surfaces. The magnitude with directions of XY, XZ, and YZ plane for (e) Young's modulus, (f) shear modulus, (g) linear compressibility, and (h) Poisson's ratio. The maximum and minimum values of shear modulus and Poisson's ratio are represented by dashed and solid lines, respectively.

3.5. Stacking fault probability

The SFP measures the amount of stacking faults formed during deformation and allows the determination of the stacking fault energy (SFE) [11,13] of the alloy. The detailed procedure of SFP and SFE calculations can be found in Section 2 of the Supplementary Materials. The measured SFP evolution of the FeNiCr alloy at 293 K and 15 K is compared with another HEA ($FeCoCrNiMo_{0.2}$) (Fig. 8(a)) [3]. At high strain levels, the $FeCoCrNiMo_{0.2}$ showed a very high level of SFP. It can reach 2.9×10^{-2} at 77 K and even increase to 5.1×10^{-2} at 15 K. The alloy has a very low SFE of 17 mJ m^{-2} and 11 mJ m^{-2} at 77 and 15 K, respectively. By contrast, the SFP of FeNiCr alloy is very low (below 7×10^{-3}) at both temperatures. According to Eq. (S13), the SFE of the alloy was estimated to be 63 ± 4 mJ m^{-2} at 293 K and 47 ± 3 mJ m^{-2} at 15 K.

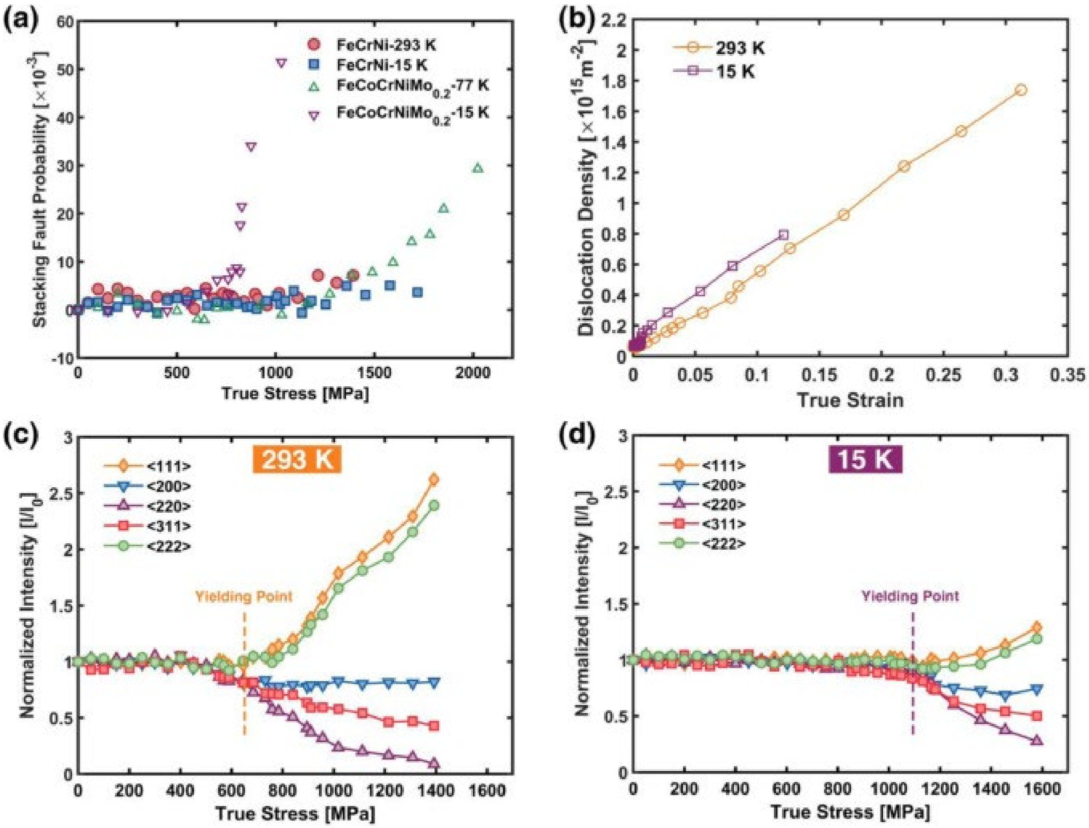

Fig. 8. Microstructure evolution during straining at 293 K and 15 K: (a) comparison of stacking fault probability (SFP) evolution between the FeNiCr alloy and $FeCoCrNiMo_{0.2}$ alloy at different temperatures; (b) dislocation density evolution of the FeNiCr alloy during deformation; the normalized peak intensity evolution of {111}, {200}, {220}, {311}, and {222} of the FeNiCr alloy during deforming at (c) 293 K and (d) 15 K.

Generally, the SFE of an alloy serves as one of the most crucial parameters determining the dominant deformation mechanisms. The strain hardening effects were mainly controlled by dislocation motion when the SFE exceeds 45 mJ m^{-2}. As the SFE decreases to the range of 18–45 mJ m^{-2}, twinning is preferable to occur. While phase transformation, from the parent FCC to newborn phases with hexagonal close-packed (HCP) and/or body-centered tetragonal (BCT) structures may occur if the SFE is further decreased to be lower than 18 mJ m^{-2} [11,22,59]. The thermodynamic calculation results indicate that the SFE of the FeNiCr alloy is in the range of 50–60 mJ m^{-2} [59]. This is also confirmed in Refs. [5,21], where the high SFE of the FeNiCr was predicted to be > 50 mJ m^{-2} by large-scale atomic simulations. These previous studies agree with our calculation based on the diffraction data analysis. The high SFE of the FeNiCr alloy (63 ± 4 mJ m^{-2} at 293 K and 47 ± 3 mJ m^{-2} 15 K) suggests that its deformation behavior is mainly controlled by the dislocation motion, while the stacking fault, twins, and phase transformation are less likely to operate during deformation. This also means that the alloys are kept as non-magnetic during deformation at very low temperatures, which is favorable for applications in super-strong magnets.

The high SFE of the FeNiCr alloy can be attributed to two reasons: (1) the low configurational entropy and (2) the high concentration of Cr and Ni. Zaddach et al. [5] applied diffraction methods and first-principles calculations to investigate the SFE of a series of MCAs (FeCoNiCrMn) and the results indicated that the SFE decreases with the increase of element complexity, i.e., constituent number or configurational entropy. On the other hand, Ref. [60] indicates that the SFE of an alloy is the combined effect of each constituent element. The same element can influence the SFE differently in different alloy systems. For the FeCoNiCrMn alloy system, the SFE can be increased by increasing Ni contents due to the high intrinsic SFE of Ni (∼125 mJ m^{-2}) [61]. This also agrees with the study of Bonny et al. [21], which suggests that the SFE of FeNiCr alloy can be significantly increased by increasing Cr and Ni contents.

3.6. Dislocation density evolution

The dislocation density evolution of the alloy during deformation was calculated with the modified Williamson–Hall method [62]. The detailed procedure for dislocation density calculation can be seen in Section 3 of the Supplementary Materials. The calculated dislocation density against true strain at both temperatures is shown in Fig. 8(b). The evolution of dislocation density showed a very similar pattern at both temperatures. The dislocation density fluctuated slightly at around 6×10^{13} m^{-2} before yielding, after which both curves increased almost linearly upon further straining. At 293 K, the dislocation density of 1.74×10^{15} m^{-2} was achieved at the true stress of 1392 MPa and the true strain of 0.31. At 15 K, the dislocation density reached 7.93×10^{14} m^{-2} at the true stress of 1576 MPa and the true strain of 0.12.

Meanwhile, the dislocation evolution is closely related to the texture development during tensile loading. The intensity of each reflection (〈111〉, 〈200〉, 〈220〉, 〈311〉, and 〈222〉) was normalized with that of the stress-free state and their evolution with true stress at 293 and 15 K are shown in Fig. 8(c, d), respectively. At both temperatures, the peak intensity curves changed very little during the elastic stage while they started to vary after the yielding points. This originates from the difference in grain rotation in response to external loading. At 293 K, after yielding, (111)//LD and (222)//LD orientated grains gradually rotated towards the loading direction, making their peak intensity increase almost linearly with the increase of true stress during subsequent straining. By contrast, the intensity of (200) peak was maintained at a similar level of ~0.8 after a slight dropping. The intensity of the other two peaks, (311) and (220), decreased to 0.43 and 0.09, respectively, as grains with these orientations gradually rotated away from LD. A similar phenomenon was also observed at 15 K (Fig. 8(b)) and reported in Refs. [3,13]. In the present work, the (111)//LD texture was used as a measure of the dislocation activity as the texture development is characteristic of dislocation slip during plastic deformation [12]. The highest (111) intensity reached 2.62 at 293 K, compared with a much lower value of 1.29 at 15 K. Meanwhile, at 293 K, the texture developed at a faster pace (with a slope of $\sim 2.35 \times 10^{-3}$ MPa^{-1}) than that at 15 K (with a slope of $\sim 0.67 \times 10^{-3}$ MPa^{-1}). The slow texture change at 15 K also explains the lower strength enhancement after yielding and deterioration of the ductility observed at 15 K (Fig. 3). The inactive grain rotation and slow texture evolution limited the dislocation motions to well-orientated grains and led to the inability of catering to larger external strain [63]. Meanwhile, fewer slip systems can be activated in those “not-so-good-oriented” grains, leading to a much lower dislocation density achieved at 15 K. This result is in good agreement with the mechanical performance (Fig. 3(a)) and the dislocation density evolution (Fig. 8(b)).

3.7. TEM characterization of the strained samples

To further reveal the underlying deformation mechanisms, post-mortem TEM characterizations were performed on the fractured samples deformed at 293 and 15 K. The bright-field TEM images were taken at a two-beam condition while the SAED patterns of the corresponding area were collected along 〈110〉 zone axis and attached to the image. Fig. 9(a) shows the bright-field STEM micrograph of the alloy deformed to a low strain level of ∼0.1 at 293 K. Massive parallel shear bands traveling through the whole grain interior were observed. The image on the inset of Fig. 9(a) is the SAED pattern taken from the area highlighted by the yellow circle, showing the matrix still maintained an FCC structure. The shear bands mainly consisted of closely arrayed dislocation walls whereas no SFs or twins were detected, indicating the alloy deformed by typical planar dislocation glide on {111} planes. The shear bands were magnified in Fig. 9(b), showing that the dislocation walls consisted of massive dense parallel primary {111} slip traces. Fig. 9(c) is the bright-field TEM image taken from the sample sectioned near the fracture surface. Dense dislocation networks were produced between slip traces. Secondary {111} slip occurred and intersected with the primary slip traces, separating the matrix into small parallelogram blocks. No SFs or twins were formed according to the corresponding SAED patterns. The mean free path of mobile dislocations can be effectively reduced by the concentrated slip bands.

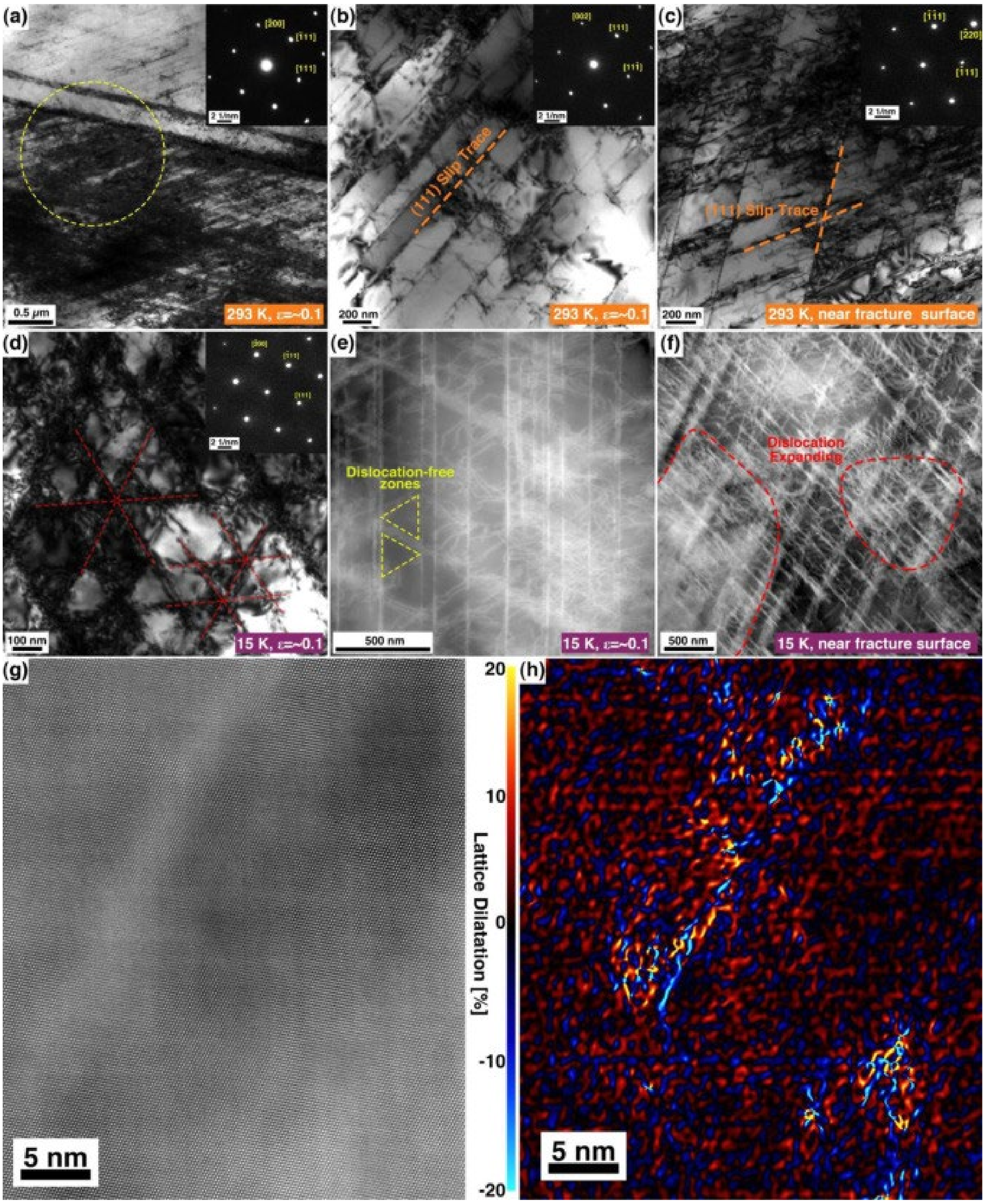

Fig. 9. Deformed microstructure of the alloy at different strain levels and different temperatures, 293 K and 15 K: (a) typical bright-field TEM image (at the strain of ~0.1, 293 K) and corresponding SAED pattern of the area marked by the yellow dashed circle; (b) and (c) bright-field TEM images and corresponding SAED patterns at the strain of 8C0.1 and near the fracture surface at 293 K, respectively; (d) bright-field TEM image and corresponding SAED pattern at the strain of ~0.1, 15 K; (e) and (f) HAADF-STEM images of the deformed structure at the strain of ~0.1 and near the fracture surface at 15 K, respectively; (g) HRTEM image of the dislocation tangling zone in (e); (h) the geometric phase analysis (GPA) conducted on (g).

Similar dislocation motions were also observed at 15 K. Fig. 9(d) is the bright-field TEM image and corresponding SAED pattern showing the microstructure of the alloy deformed to a strain of ~0.1 at 15 K. Comparing with Fig. 9(b), the secondary slip system is more easily activated at 15 K, and more dislocation tangling kinks were observed. Dislocations were preferably gathered around the crossing slip systems and formed parallelogram blocks. The interior of the nanosized dislocation substructure shows a relatively lower dislocation density than the block boundaries. The morphologies of dislocation networks deform to a strain of ~0.1 and near the fracture surface were further revealed by STEM-HAADF images in Fig. 9(e, f), respectively. The while lines were identified as dislocation traces according to the HRTEM image (Fig. 9(f)). In Fig. 9(f), the density of intersecting active slip planes increased significantly as more slip systems were activated, refining the spacing between coplanar slip bands significantly. The concentrated slip bands can hinder dislocation slip on parallel slip bands by increasing the passing stresses. Furthermore, rapid dislocation multiplication occurs in both dislocation walls and the small dislocation-free zones (Fig. 9(e)), thickening the dislocation walls effectively and gradually expanding dislocations to the whole block interior (Fig. 9(f)). Fig. 9(g) displays the HAADF image of a slip trace junction in Fig. 9(f, h) is the lattice dilatation resulting from the presence of a high strain field, obtained from the trace of the lattice distortion matrix via the GPA method [47]. This result identified the crossing slip traces, especially their junctions, mainly consisted of tangling dense dislocations accompanied by a high residual strain field. It is also worth noting that at both temperatures, very few short and isolated stacking faults were observed from our STEM observation, which is consistent with our neutron diffraction results in Fig. 8(a).

4. Modeling results

In this section, we used density functional theory calculation to identify SRO and determine the single-crystal elastic constants, which were compared against experimental results. Via dislocation-based slip system modeling with key parameters taken from the neutron diffraction data, we were able to determine strengthening sources contributing to the yield strength, and the underlying factors controlling strain hardening during plastic deformation for the FeCrNi alloy.

4.1. Phase formation parameters

Several thermodynamic parameters related to phase formation including ΔSmix (entropy of mixing), ΔHmix (enthalpy of mixing), and Tm (melting point) were calculated (see Section 5 in the Supplementary Materials). Beside, the parameter Ω, which can be applied to predict the solid-solution formation of random MCAs, was calculated according to Ref. [64]:(5)Ω=TmΔSmix|ΔHmix|

When Ω >1, the MCAs are mainly composed of solid solutions while Ω ≤1, the formation of intermetallic compounds or segregations is favored.

Another important parameter in predicting the solid-solution formation is the parameter δ [64], which describes the atomic size difference of the MCAs and can be expressed as follows Eq. (6):(6)δ=∑i=1nci(1−rir¯)2where ri is the atomic radius and r¯=∑i=1nciri is the average atomic radius. According to Refs. [64,65], when $\Omega \geq 1.1$ and $\delta \leq 6.6\%$, stable solid-solution phases can be formed in MCAs.

Furthermore, Guo and Liu [66] indicated that the valence electron concentration (VEC) serves as a criterion for determining the lattice structure of the MCAs as it correlated a structure's VEC with its FCC/BCC phase formation. It is defined by:(7)VEC=∑i=1nci(VEC)i,where (VEC)i is the VEC for *i*th element and can be found at Ref. [66]. When VEC ≥ 8, FCC structure is more stable while VEC ≤ 6.87, BCC phases are more stable.

Therefore, multiple phase formation parameters can be calculated based on Eqs. (5)–(7) and the results are shown in Table 4. As can be seen, the FeCrNi alloy has a very high ΔSmix (9.132 J K^{-1} mol^{-1}), Tm (1906.6 K), and relatively small ΔHmix (–4.3972 KJ mol^{-1}), yielding the high value of Ω (3.9596). Accompanied with a low δ value (only 0.002), the result indicates that the alloy can favorably form stable solid-solution phases. Additionally, the VEC of the alloy is calculated to be 7.97, which is very close to the theoretical criterion of forming a single FCC structure [66]. According to the neutron diffraction spectrum (Fig. 3) and TEM results (Figs. 2 and 9), a single FCC solid solution phase was observed, in good agreement with the theoretical prediction.

4.2. DFT results

According to the DFT results, up to the melting point, the free energy calculations considering magnetic corrections demonstrate that the FCC phase is stable at the equiatomic composition of FeCrNi alloy, which is in excellent agreement with the available experimental data. The atomistic configurations of medium-range and equiatomic FeCrNi alloys obtained from the present Monte Carlo (MC) simulations of the 9 × 9 × 9 FCC supercell for two temperatures: 300 and 2000 K are shown in Fig. 1(a, b), respectively. At 2000 K, the configuration is more related to a disordered distribution of Fe, Cr, and Ni atoms over the simulation cell, whereas, at 300 K, the configuration is more related to an ordering configuration. To understand this disorder-to-order transition, Fig. 10 shows the dependence of the first nearest-neighbor (1NN) SRO parameters of Fe-Cr, Fe-Ni, and Cr-Ni pairs as a function of temperature. At the high-temperature region, all the values of SRO trend to approach the zero values corresponding to random alloy configurations. For the region of temperature lower than 1000 K, it is found that the SRO parameters for Fe-Cr and Fe-Ni are negatively expressing the chemical interactions between these pairs in the ternary FeCrNi alloy. Between them, the SRO parameters for Fe-Cr pairs are more negative than those of Fe-Ni, demonstrating a stronger chemical ordering between Fe and Cr. The SRO parameters between Cr and Ni are positive in this temperature range, demonstrating that these two atoms did not like each other within the 1NN shell of the FCC lattice.

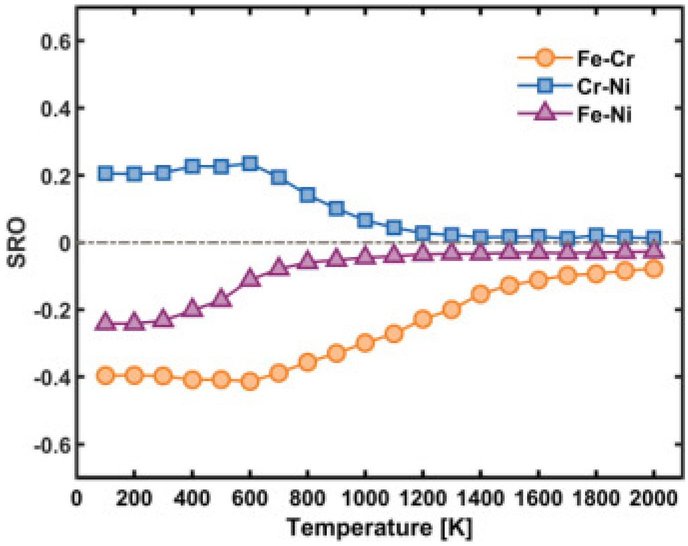

Fig. 10. Dependence of SRO parameters as a function of temperature between the three different pairs in equiatomic FeCrNi alloys.

Fig. 1(c, d) shows the 3 × 3 × 3 supercell configurations used for DFT calculations of elastic constants in equiatomic FeCrNi alloys within the present work. They were generated by using combined first-principles CE Hamiltonian with exchange Monte Carlo simulations at 300 and 2000 K. Space group symmetry of these configurations are found to be *P*1 and *Pnnm*, respectively. The prediction of orthorhombic symmetry for the 300 K configuration demonstrates that the ordered structure obtained from the present theoretical study is strongly correlated with the SRO effects shown in Fig. 10 at low temperature for the medium-range FeCrNi alloy with equiatomic composition. It is worth noting that the point group symmetry of *Pnnm* crystal represents a subgroup of the tetragonal structure *P*4/*mmm* which has been previously predicted for intermetallic phase Fe_2CrNi from our DFT study in the FCC Fe-Cr-Ni system [35].

The elastic constants calculated by DFT for configurations generated by MC simulations at 300 and 2000 K MC are shown in Table 3. Note that for the high-temperature (2000 K) configurations with *P*1 symmetry, the elastic constant values were computed by the new method outlined from Eqs. (3) and (4) where the 12 components from 21 independent elastic tensor components are negligible for the random alloy configuration. For the low-temperature configuration (300 K), DFT calculations provide 9 independent elastic constant values according to the orthorhombic group symmetry *Pnnm*. The optimized lattice constants from DFT calculations for the low-temperature configurations are $a = 3.5549$ Å, $b = 3.5486$ Å, and $c = 3.6264$ Å which are slightly different from the ones for a cubic cell. The corresponding values for high-temperature configurations are $a = 3.5385$ Å, $b = 3.5459$ Å, and $c = 3.5722$ Å. A larger lattice constant value at low temperature can be explained by magneto-volume effects due to high values of predicted magnetic moments in the ordered FeCrNi alloys. According to our DFT calculations, the average ferromagnetic moments of Fe and Ni sites are 2.1 and 0.16 μ_B, respectively, whereas an average anti-ferromagnetic moment of ±2.2 μ_B is found from Cr sites within the orthorhombic structure *Pnnm*. Note that the magnetic moment value predicted for the Fe site in the Fe_2CrNi structure is also found to be close to 2.1 μ_B [35]. For the high-temperature configuration, magnetic moments at different atomic sites are found to be randomly distributed and their average values are smaller than those predicted above for the ordered structure as expected. As it can be seen from Table 3, the DFT calculations were performed within different options, either with the lattice and ionic relaxations (denoted as “Relaxed”) or without ionic relaxations (denoted as “Unrelaxed”).

From the DFT results, it is found that elastic constants at high temperatures are smaller than the ones under low-temperature configurations, demonstrating the strong effect of disorder with respect to chemical ordering for the latter one. From Table 3, the predicted DFT elastic properties for the disordered configuration generated by MC simulations at 2000 K are in very good agreement with the experimental values measured in this work. The elastic properties obtained by DFT are shown in Fig. 7(i–l), which also closely resembles those measured experimentally. This strongly indicates that the prepared experimental FeCrNi alloy samples are more likely to be in a metastable state as a result of the fabrication (fast cooling after hot extrusion) without annealing treatment, which may prevent the formation of SROs and ordered intermetallic phase predicted by DFT calculations at a low-temperature regime [15,16]. This means that the SRO effects shown in Fig. 10 from our modeling work are absent in the present experimental alloys. The absence of the SRO effect was checked by the neutron diffraction results (Fig. 4) and it is found that no other diffuse superlattice peaks can be identified experimentally. Furthermore, this result is well supported by the APT analysis and the extensive HRTEM analysis (Fig. 2). SRO formation preferably occurred after long-time annealing at high temperatures. For example, in CrCoNi alloy, SROs were observed after annealing at 1000 °C for 120 h [16].

4.3. Yield strength modeling

For the FeNiCr MEA, the YS can be the accumulative result of several strength contributors including frictional stress (σfr), initial dislocation density (σdis), precipitate hardening (σppt), grain boundary strengthening (σgb), and SRO strengthening (σSRO) Eq. (8) [2]:(8)$\sigma YS=\sigma fr+\sigma dis+\sigma ppt+\sigma gb+\sigma SRO$

First, the precipitation strengthening can be ignored in the present study. According to the neutron diffraction results shown in Fig. 4, during elastic deformation at both 293 and 15 K, the alloy keeps a single FCC phase, and no precipitates were detected except a small amount of Cr-rich phases at grain boundaries (Fig. 2(c)). The bright-field TEM images and corresponding SAED patterns (Figs. 2 and 9) do not reveal nano-precipitates. Next, we address the SRO hardening effects. On one hand, the HRTEM characterization in Fig. 2 indicates only a trace amount of SRO may be present. On the other hand, the strengthening effects of SRO can be very limited according to Ref. [67]. Therefore, the strengthening effects of trace SRO in the MEA can be neglected.

The strengthening contribution from forest dislocations can be evaluated by the classic Taylor hardening model Eq. (9) [68]:(9)$\sigma dis=M\alpha Gb\rho$,where M is the Taylor factor and equals 3.06 for an FCC polycrystalline matrix, α is a constant of 0.35 [69] related to the interaction strength between dislocations, G is the shear modulus, b is the Burger's vector, and ρ is the dislocation density. The neutron diffraction results indicate that the dislocation density of the virgin sample is around 6×10^{13} m^{-2} at both 293 and 15 K (Fig. 8(b)). According to Eq. (9), the strengthening effects from initial dislocations are ∼164 MPa at 293 K and ∼196 MPa at 15 K.

The strengthening effect of grain boundaries (σgb) can be calculated via the Hall–Petch equation. The grain boundary strengthening effect keeps a linear relationship with the inverse square root of average grain size Eq. (10) [70]:(10)$\sigma gb=G(T)G(RT)Kgbd-1/2$where the Hall–Petch coefficient (K_{gb}) of 0.966 MPa·$m^{1/2}$ was used based on Ref. [6], G(T)and G(RT)are the shear modulus at the given temperature and room temperature, respectively. With the average grain size of ∼23.4 μm, the grain boundaries contributed ∼200 MPa (293 K) and ∼218 MPa (15 K) to the yield stress.

Next, we address the lattice friction stress (σfr) of the alloy at the two temperatures. Note that the classical solid-solution strengthening mechanism is limited to the conventional ductile alloy systems where the dislocation movement can be inhibited by the strain field arising from the mismatch between discrete and solvent atoms [7]. The flexibility of dislocation lines enables them to bend to overcome the energy barriers and take on low-energy configurations. However, as the notion of “one principal element” was abandoned in MCAs, the constituent atoms with different sizes can be randomly distributed among the matrix, in which each elemental atom in the alloys can act as a solute. In this scenario, the traditional “solvent” lattice does not exist and the spacing distance between each energy barrier can be decreased significantly [4,18]. Thus, the traditional methods of depicting lattice friction stress and solution strengthening effects are no longer suitable for MCAs. According to Ref. [2], the MCAs can be treated as a stoichiometric compound with a fixed atomic ratio albeit disordered. Therefore, the traditional solid solution hardening contribution can be included in the lattice friction effect, which can be more representative of the averaged lattice resistance provided by all types of constituent elements.

Recently, Varvenne et al. [18] proposed a general mechanistic solute strengthening theory (here named as the Varvenne-Luque-Curtin theory) for arbitrary MCAs, showing great success in predicting the YS of multiple HEAs and MEAs by correlating composition, temperature, and strain rate [19]. Different from traditional solute strengthening effects, the Varvenne-Luque-Curtin theory assumes that the MCA is an effective-medium matrix having all the average properties of the alloy. Each substitutional element is treated as a solute embedded in the matrix and serves as local fluctuation. The strengthening effect then originates from the rising fluctuating interaction energies between dislocations and dense local fluctuations. To reduce the total potential energy, the dislocation adopts a wavy configuration and is locally pinned in a low-energy region. The representative wavy configuration of dislocations was observed in the slightly deformed samples at 15 K (as shown in Fig. S2 in the Supplementary Materials), where the dislocation motion shows sluggish features, indicating high resistance originating from the pronounced lattice distortion in MCAs [16]. With the aid of stress-assisted thermal activation, the trapped dislocation can escape the adjacent energy well and reach the next low-energy region along the dislocation gliding plane. This theory calculated the zero-temperature flow stress (τy0) and fundamental zero-stress energy barrier (ΔEb) at finite temperature (T) and finite strain-rate (ε˙), according to Eq. (11) and Eq. (12), respectively [18]:(11)τy0=Aταt−13G(1+v1−v)43[∑ncnΔVn2b6]23(12)ΔEb=AEαt13 Gb3(1+v1−v)23[∑ncnΔVn2b6]13where Aτ=0.04865[1−(A−1)40] and AE=2.5785[1−(A−1)80] are two constants related to the core structure of FCC dislocations consisting of two separated partial dislocations accompanied with a correction for elastic anisotropy with the Zener anisotropy factor A=2C44(C11−C12). αt=0.125is a dimensionless line tension parameter for FCC alloys [19]. ΔVnis the misfit volume of a type-*n* element at composition (cn) in the alloy and can be calculated by Eq. (13) [4]:(13)ΔVn=∂Valloy∂cm−∑mNcm∂Valloy∂cmwhere Valloy=Valloy(c1, c2,...,cN−1)is the atomic volume of the alloy and ∂Valloy∂cN=0. The volume misfit can then be experimentally determined by measuring the lattice parameter evolution over a series of alloys [19]. It can also be computed precisely with the first-principles calculation, after replacing one type-*n* atom multiple times with a type-*m* atom at many different atomic environments [71]. In our case, we applied Vegard's law (Valloy=∑ncnVn) to estimate the misfit volume (Eq. 14) [4,18]:(14)ΔVn=Vn−Valloywhere Vn is the apparent volume of the type-*n* element. Based on the experimental results on Ni, Ni-Cr, and Ni-Fe binary alloys from Ref. [18], the apparent atomic volumes of the three constituent elements Fe, Cr, and Ni were adapted to be 12.09, 12.27, and 10.94 Å^3, respectively.

At finite temperature *T* and finite strain-rate, Eqs. (11) and (12) can be combined to Eq. (15), based on the standard thermal activation [72]:(15)τy(T,ε˙)=τy0exp(−10.51kBTΔEb(T)lnε˙0ε˙)where the strain rate (ε˙) of 8 × 10^{-5} s^{-1} was used in the present work, ε˙0 is the reference strain rate and a value of 10^4 s^{-1} was adapted according to Refs. [18,19], and kBis the Boltzmann constant. Therefore, the uniaxial friction stress (σ_{fr}) can then be calculated by multiplying the shear stress (τ_y) by the Taylor factor using Eq. (16):(16)σfr(T,ε˙)=Mτy(T,ε˙)

Finally, with inputs obtained from the experiments (Tables 3 and 5), the lattice friction stress of the FeCrNi alloy was determined to be 316 and 629 MPa at 293 and 15 K, respectively.

According to Eq. (8), the YS of the alloy at 293 and 15 K can be estimated to be 680 and 1043 MPa, respectively. As compared in Table 5, the modeled strength shows acceptable agreement with the measured results at both temperatures. The calculation of strengthening contribution from lattice distortion based on the Varvenne-Luque-Curtin theory of random MCAs plays a critical role in understanding the strengthening mechanisms and can serve as a guideline in designing and optimizing new MCAs.

4.4. Plastic deformation

Generally, the large elongation of FCC alloys can be achieved via introducing extra strengthening mechanisms (such as TWIP and TRIP effects) [22]. The FeCrNi has high SFE and no TWIP or TRIP effects were observed when deformed. The high SFE of the

FeCrNi MEA means that the activation of multiple strengthening mechanisms is impeded. Hence, the dislocation activity becomes the main strain contributor during the plastic deformation [11,22,59]. Even with the only dislocation strengthening for the FeCrNi, a notably good combination of strength and ductility was obtained. This result further augments the recent research of Luo and Huang [73] showing that TWIP and TRIP are not necessarily required for extra-large ductility. The large ductility (48%) at 293 K might be attributed to divisive slip systems activated and the high dislocation multiplication capacity of the alloy. According to the diffraction results (very low level of SFP, high SFE, and no twinning and phase transformation during deformation), together with the post-deformation TEM observations (Fig. 9), the dislocation motion and multiplication are the main strengthening resource and carrier of plasticity during plastic deformation.

Based on dislocation motions, the deformation procedure at 293 and 15 K was schematically compared in Fig. 11. At 15 K, grain rotation from other orientations to (111)//LD develops much slower than that at 293 K (Fig. 8(c, d)). A similar phenomenon can also be observed in another MEA of CrCoNi during deforming at 15 K [56]. Grains orientated near (111)//LD were highly strained and dislocation entanglement formed more easily, leading to the deterioration of the ductility. Beside, the low temperature also impeded the dislocation motion, especially dislocation annihilation, contributing to the faster dislocation increment at 15 K (Fig. 8(b)) [22]. While at 293 K, the rapid growing texture endowed not-so-good-orientated grains with the ability to activate more slip systems, and thus, providing extra strain carriers. This process can sustainably support dislocation multiplication, providing a stronger dislocation strengthening effect and improved ductility.

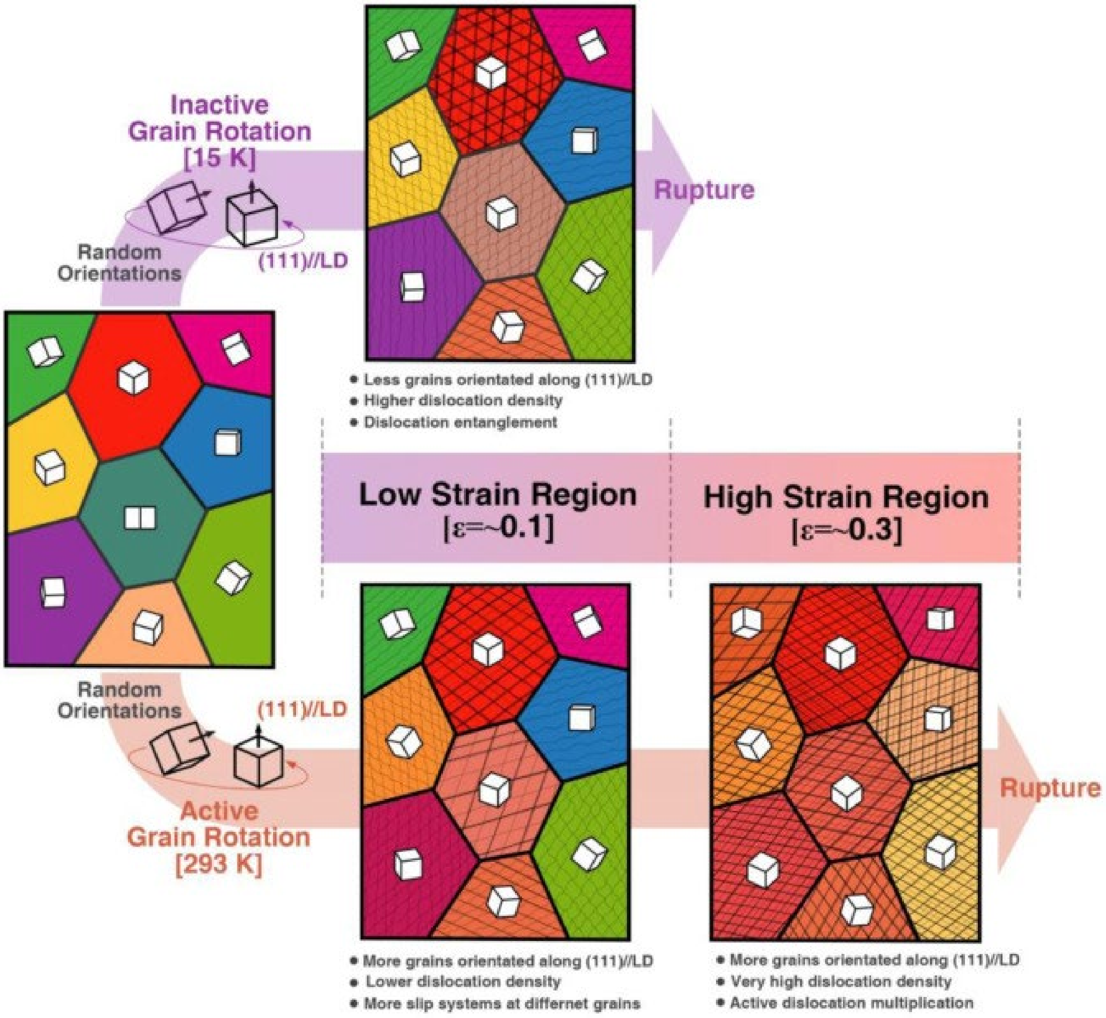

Fig. 11. Schematic illustration of the deformation procedure at 293 and 15 K.

Based on the dislocation-dominated deformation mechanism, a constitutive model to depict the total flow stress (σ) of the alloy can be derived as follows Eq. (17):(17)$\sigma=\sigma fr+\sigma gb+\sigma dis$.

The strengthening effect from dislocation can be determined by Eq. (9) and the dislocation density evolution (Fig. 8(b)). After yielding, the dislocation density increased almost linearly with the true stress at both temperatures. When deforming at 293 K to a true strain of 0.31, strengthening contribution from dislocations can reach 854 MPa. At 15 K, dislocations contributed 697 MPa at a true strain of 0.12. The accumulated strengthening contributions from different resources at 293 and 15 K according to Eq. (17) are compared with the measured flow stress at 293 and 15 K as shown in Fig. 12(a, b), respectively. The model calculations agree very well with the experimental results.

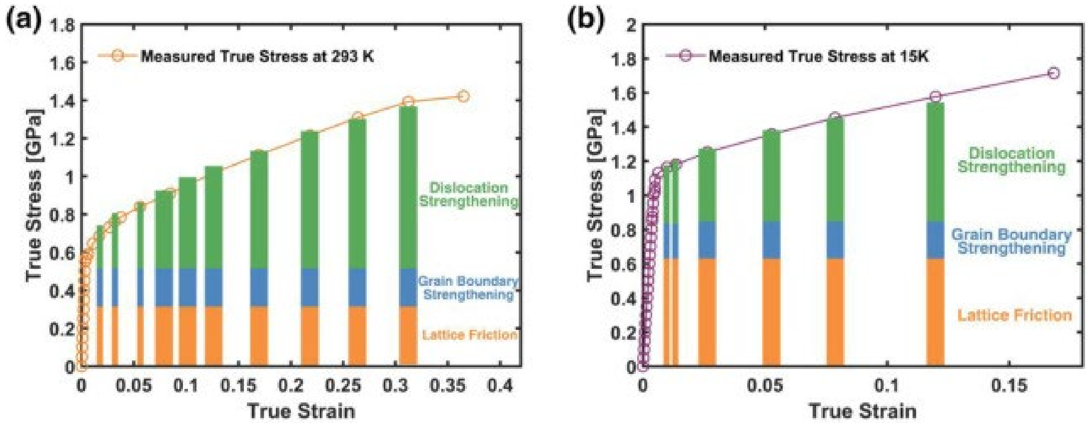

Fig. 12. Comparison between the calculated strength originating from different strengthening resources and the measured total flow stress at (a) 293 K and (b) 15 K.

5. Conclusions

In this study, we have investigated the deformation behaviors and strengthening mechanisms of an equiatomic ternary FeNiCr MEA at 293 K and 15 K. *In situ* neutron diffraction and theoretical simulations (DFT and dislocation slip system driven modeling) were synergistically employed to (i) map the microstructure evolution (e.g., lattice strain, SFP, and dislocation density); (ii) determine key mechanistic parameters (single crystal elastic constants and SFE); and (iii) confirm the strengthening mechanisms. The investigation leads to the following conclusions:

(1)The equiatomic ternary FeNiCr alloy showed excellent strength–ductility balance at 293 K with a YS of 651 ± 12 MPa, a UTS of 1020 ± 3 MPa, and a total elongation of 48% ± 5%. At 15 K, ultrahigh YS of 1092 ± 22 MPa and UTS of 1451 ± 2 MPa were achieved, while the elongation decreased to 18% ± 1%.

(2) MC simulation predicts the formation of short-range ordering and Fe2CrNi intermetallic. However, no short-range orderings were observed according to the neutron diffraction spectra and APT. TEM analysis shows a very small amount of short-range ordering might be present. This indicates that the alloy is at a metastable state and the SRO effect is almost absent possibly due to the sample fabrication technique used.

(3) Single-crystal elastic constants and bulk elastic moduli were calculated from the neutron diffraction data, which agree well with the DFT simulation for the disordered configuration generated by MC simulations at 2000 K, but less well with the ordered configuration generated by MC at 300 K. This again suggests that the alloy produced is in a metastable configuration.

(4) At both 293 and 15 K, the FeNiCr MEA showed high phase stability and maintained as an FCC solid solution during deformation. Meanwhile, it showed a very low level of stacking fault probability during deformation and had high SFE (63 ± 4 mJ m^{-2} at 293 K and 47 ± 3 mJ m^{-2} at 15 K), indicating its inability of producing dense stacking faults and introducing TWIP and TRIP effects. The *in situ* neutron diffraction data and TEM analysis confirmed that no TWIP or TRIP effects occurred when the alloy was

deformed at both temperatures.

(5) The high solute misfit volumes of the FeNiCr can effectively introduce severe lattice distortion, which substantially improves the yield strength, especially at extremely low-temperature conditions. Based on the Varenne-Luque-Curtin theory, the strengthening contribution from the lattice distortion was calculated. At 293 K, the friction stress, resulting from the lattice distortion, can contribute 316 MPa to the YS, while it increased significantly to 629 MPa at 15 K. Strengthening contributions from dislocation and grain boundaries were also calculated. And the sum of the three contributions agreed well with the measured yield strength at both temperatures.

(6) During plastic deformation, dislocation motion and multiplication served as the dominant deformation mechanism and the main strain carrier at 293 and 15 K. The as-fabricated samples had a low dislocation density of $\sim 6 \times 1013\ \mathrm{m}^{-2}$. After yielding, dislocation density increased almost linearly with true stress.

Declaration of Competing Interest

The authors declare that they have no known competing financial interests or personal relationships that could have appeared to influence the work reported in this paper.

Acknowledgement

The authors thank ISIS neutron and muon source (the Rutherford Appleton Laboratory, UK) for providing the beamtime (RB1810732 and RB1920111) and staff at ENGIN-X beamline for support. Atom probe tomography research was conducted by Dr. J.H. Luan and Dr. Z.B. Jiao at the Inter-University 3D Atom Probe Tomography Unit of City University of Hong Kong, which is supported by the CityU grant 9360161 and RGC grant 25202719. DNM's work has been carried out within the framework of the EUROfusion Consortium and has received funding from the Euratom research and training programs 2014–2018 and 2019–2020 under Grant Agreement No. 633053 and from the RCUK Energy Programme [Grant No. EP/T012250/1]. We also acknowledge funding from the European Research Council (ERC) under the European Union's Horizon 2020 research and innovation program (grant agreement No. 714697). The views and opinions expressed herein do not necessarily reflect those of the European Commission. DNM and JSW acknowledge the support from high-performing computing facility MARCONI (Bologna, Italy) provided by EUROfusion. The work at Warsaw University of Technology has been carried out as a part of an international project co-financed from the funds of the program of the Polish Minister of Science and Higher Education entitled "PMW" in 2019, Agreement No. 5018 / H2020-Euratom / 2019/2. The simulations were also carried out with the support of the Interdisciplinary center for Mathematical and Computational Modeling (ICM), University of Warsaw, under grant No. GB79–6.

References

[1] J.W. Yeh, S.K. Chen, S.J. Lin, J.Y. Gan, T.S. Chin, T.T. Shun, C.H. Tsau, S.Y. Chang, Adv. Eng. Mater. 6 (2004) 299–303.

[2] Z. Wu, H. Bei, G.M. Pharr, E.P. George, Acta Mater. 81 (2014) 428–441.
[3] B. Cai, B. Liu, S. Kabra, Y. Wang, K. Yan, P.D. Lee, Y. Liu, Acta Mater. 127 (2017) 471–480.
[4] B. Yin, F. Maresca, W.A. Curtin, Acta Mater. 188 (2020) 486–491.
[5] A.J. Zaddach, C. Niu, C.C. Koch, D.L. Irving, JOM 65 (2013) 1780–1789.
[6] M. Schneider, G. Laplanche, Acta Mater. 204 (2020) 116470.
[7] S.S. Sohn, A. Kwiatkowski da Silva, Y. Ikeda, F. Körmann, W. Lu, W.S. Choi, B. Gault, D. Ponge, J. Neugebauer, D. Raabe, Adv. Mater. 31 (2019) 1–8.
[8] Z. Li, K.G. Pradeep, Y. Deng, D. Raabe, C.C. Tasan, Nature 534 (2016) 227–230.
[9] B. Gludovatz, A. Hohenwarter, D. Catoor, E.H. Chang, E.P. George, R.O. Ritchie, Science 345 (2014) 1153–1159.
[10] B. Gludovatz, A. Hohenwarter, K.V.S.S. Thurston, H. Bei, Z. Wu, E.P. George, R.O. Ritchie, Nat. Commun. 7 (2016) 10602.
[11] L. Tang, K. Yan, B. Cai, Y. Wang, B. Liu, S. Kabra, M.M. Attallah, Y. Liu, Scr. Mater. 178 (2020) 166–170.
[12] M. Naeem, H. He, F. Zhang, H. Huang, S. Harjo, T. Kawasaki, B. Wang, S. Lan, Z. Wu, F. Wang, Y. Wu, Z. Lu, Z. Zhang, C.T. Liu, X.L. Wang, Sci. Adv. 6 (2020) eaax4002.
[13] Y. Wang, B. Liu, K. Yan, M. Wang, S. Kabra, Y.L. Chiu, D. Dye, P.D. Lee, Y. Liu, B. Cai, Acta Mater. 154 (2018) 79–89.
[14] J. Ding, Q. Yu, M. Asta, R.O. Ritchie, Proc. Natl. Acad. Sci. U. S. A. 115 (2018) 8919–8924.
[15] X.F. Chen, Q. Wang, Z.Y. Cheng, M.L. Zhu, H. Zhou, P. Jiang, L.L. Zhou, Q.Q. Xue, F.P. Yuan, J. Zhu, X.B. Wu, E. Ma, Nature 592 (2021) 712–716.
[16] R. Zhang, S. Zhao, J. Ding, Y. Chong, T. Jia, C. Ophus, M. Asta, R.O. Ritchie, A.M. Minor, Nature 581 (2020) 283–287.
[17] Z. Wu, Y. Gao, H. Bei, Acta Mater. 120 (2016) 108–119.
[18] C. Varvenne, A. Luque, W.A. Curtin, Acta Mater. 118 (2016) 164–176.
[19] B. Yin, S. Yoshida, N. Tsuji, W.A. Curtin, Nat. Commun. 11 (2020) 2507.
[20] A. Fu, B. Liu, W. Lu, B. Liu, J. Li, Q. Fang, Z. Li, Y. Liu, Scr. Mater. 186 (2020) 381–386.
[21] G. Bonny, D. Terentyev, R.C. Pasianot, S. Poncé, A. Bakaev, Model. Simul. Mater. Sci. Eng. 19 (2011) 085008.
[22] L. Tang, L. Wang, M. Wang, H. Liu, S. Kabra, Y. Chiu, B. Cai, Acta Mater. 200 (2020) 943–958.
[23] G. Kresse, J. Furthmüller, Phys. Rev. B 54 (1996) 11169–11186.
[24] G. Kresse, J. Furthmüller, Comput. Mater. Sci. 6 (1996) 15–50.
[25] J.P. Perdew, K. Burke, M. Ernzerhof, Phys. Rev. Lett. 77 (1996) 3865–3868.
[26] H.J. Monkhorst, J.D. Pack, Phys. Rev. B 13 (1976) 5188–5192.
[27] D. Nguyen-Manh, D.G. Pettifor, G. Shao, A.P. Miodownik, A. Pasturel, Philos. Mag. A 74 (1996) 1385–1397.
[28] D. Nguyen-Manh, D.G. Pettifor, Intermetallics 7 (1999) 1095–1106.
[29] D. Nguyen-Manh, D.G. Pettifor, W.Y Kim, D.M. Dimiduk, M.H. Loretto, in: Gamma Titanium Aluminides, Editors Y.W. Kim, D.M. Dimiduk and M.H.

Loretto, The Mineral, Metals and Materials Society (TMS), 1999, pp. 175–182.
[30] D. Nguyen-Manh, V. Vitek, A.P. Horsfield, Prog. Mater. Sci. 52 (2007) 255–298.
[31] M. Muzyk, D. Nguyen-Manh, K.J. Kurzydłowski, N.L. Baluc, S.L. Dudarev, Phys. Rev. B 84 (2011) 104115.
[32] J. Wróbel, L.G. Hector, W. Wolf, S.L. Shang, Z.K. Liu, K.J. Kurzydłowski, J. Alloy Compd. 512 (2012) 296–310.
[33] L. Vitos, P.A. Korzhavyi, B. Johansson, Phys. Rev. Lett. 88 (2002) 155501.
[34] N. Al-Zoubi, Metals 9 (2019) 792 (Basel).
[35] J.S. Wróbel, D. Nguyen-Manh, M.Y. Lavrentiev, M. Muzyk, S.L. Dudarev, Phys. Rev. B 91 (2015) 024108.
[36] J.M. Cowley, Phys. Rev. 77 (1950) 669–675.
[37] B.E. Warren, X-ray Diffraction, Courier Corporation, 1990.
[38] A. Fernández-Caballero, J.S. Wróbel, P.M. Mummery, D. Nguyen-Manh, J. Phase Equilib. Diffus. 38 (2017) 391–403.
[39] A. Fernández-Caballero, M. Fedorov, J. Wróbel, P. Mummery, D. Nguyen-Manh, Entropy 21 (2019) 68.
[40] M. Fedorov, J.S. Wróbel, A. Fernández-Caballero, K.J. Kurzydłowski, D. Nguyen–Manh, Phys. Rev. B 101 (2020) 174416.
[41] D. Sobieraj, J.S. Wróbel, T. Rygier, K.J. Kurzydłowski, O. El Atwani, A. Devaraj, E. Martinez Saez, D. Nguyen-Manh, Phys. Chem. Chem. Phys. 22 (2020) 23929–23951.
[42] M. Łopuszy ́nski, J.A. Majewski, Phys. Rev. B 76 (2007) 045202.
[43] D. Holec, M. Friák, J. Neugebauer, P.Hc. Mayrhofer, Phys. Rev. B 85 (2012) 64101.
[44] M.A. Caro, S. Schulz, E.P. O'Reilly, J. Phys. Condens. Matter 25 (2013) 025803.
[45] J.S. Wróbel, M.R. Zemła, D. Nguyen-Manh, P. Olsson, L. Messina, C. Domain, T. Wejrzanowski, S.L. Dudarev, Comput. Mater. Sci. 194 (2021) 110435.
[46] R. Hill, Proc. Phys. Soc., Sect. A 65 (1952) 349–354.
[47] M.J. Hÿtch, E. Snoeck, R. Kilaas, Ultramicroscopy 74 (1998) 131–146.
[48] J.Y. He, W.H. Liu, H. Wang, Y. Wu, X.J. Liu, T.G. Nieh, Z.P. Lu, Acta Mater. 62 (2014) 105–113.
[49] J.B. Liu, Y.B. Jin, X.Y. Fang, C.X. Chen, Q. Feng, X.W. Liu, Y.Z. Chen, T. Suo, F. Zhao, T.L. Huang, H.T. Wang, X. Wang, Y.T. Fang, Y.J. Wei, L. Meng, J. Lu, W. Yang, Sci.
Rep. 6 (2016) 1–9.
[50] Z. Li, C.C. Tasan, K.G. Pradeep, D. Raabe, Acta Mater. 131 (2017) 323–335.
[51] H.L. Huang, Y. Wu, J.Y. He, H. Wang, X.J. Liu, K. An, W. Wu, Z.P. Lu, Adv. Mater. 29 (2017) 1–7.
[52] L. Lilensten, J.P. Couzinié, J. Bourgon, L. Perrière, G. Dirras, F. Prima, I. Guillot, Mater. Res. Lett. 5 (2017) 110–116.
[53] O.N. Senkov, S.L. Semiatin, J. Alloy Compd. 649 (2015) 1110–1123.
[54] G. Dirras, L. Lilensten, P. Djemia, M. Laurent-Brocq, D. Tingaud, J.P. Couzinié, L. Perrière, T. Chauveau, I. Guillot, Mater. Sci. Eng. A 654 (2016) 30–38.
[55] S. Sheikh, S. Shafeie, Q. Hu, J. Ahlström, C. Persson, J. Veselý, J. Zýka, U. Kle-

ment, S. Guo, J. Appl. Phys. 120 (2016) 164902.

[56] H. He, M. Naeem, F. Zhang, Y. Zhao, S. Harjo, T. Kawasaki, B. Wang, X. Wu, S. Lan, Z. Wu, W. Yin, Y. Wu, Z. Lu, J.J. Kai, C.T. Liu, X.L. Wang, Nano Lett. 21 (2021) 1419–1426.

[57] J. Sas, K.P. Weiss, A. Jung, IOP Conf. Ser. Mater. Sci. Eng. 102 (2015) 012003.

[58] C. Lee, G. Kim, Y. Chou, B.L. Musicó, M.C. Gao, K. An, G. Song, Y.C. Chou, V. Kep-pens, W. Chen, P.K. Liaw, Sci. Adv. 6 (2020) eaaz4748.

[59] S. Curtze, V.T.T. Kuokkala, Acta Mater. 58 (2010) 5129–5141.

[60] L. Vitos, J.O. Nilsson, B. Johansson, Acta Mater. 54 (2006) 3821–3826

[61] C.B. Carter, S.M. Holmes, Philos. Mag. 35 (1977) 1161–1172.

[62] T. Ungár, S. Ott, P.G. Sanders, A. Borbély, J.R. Weertman, Acta Mater. 46 (1998) 3693–3699.

[63] W.F. Hosford, Mechanical Behavior of Materials, Cambridge University, 2005 Ph.D Thesis.

[64] X. Yang, Y. Zhang, Mater. Chem. Phys. 132 (2012) 233–238.

[65] M. Zhang, L.G. Hector, Y. Guo, M. Liu, L. Qi, Comput. Mater. Sci. 165 (2019) 154–166.

[66] S. Guo, C.T. Liu, Prog. Nat. Sci. Mater. Int. 21 (2011) 433–446.

[67] R. Zhang, S. Zhao, C. Ophus, Y. Deng, S.J. Vachhani, B. Ozdol, R. Traylor, K.C. Bustillo, J.W. Morris, D.C. Chrzan, Sci. Adv. 5 (2019) eaax2799.

[68] O. Bouaziz, S. Allain, C. Scott, Scr. Mater. 58 (2008) 484–487.

[69] R. Madec, B. Devincre, L.P. Kubin, Phys. Rev. Lett. 89 (2002) 1–4.

[70] J.P. Hirth, J. Lothe, Theory of Dislocations, Krieger Publishing Company, Florida, 1982.

[71] B. Yin, W.A. Curtin, NPJ Comput. Mater. 5 (2019) 1–7.

[72] G.P.M. Leyson, L.G. Hector, W.A. Curtin, Acta Mater. 60 (2012) 3873–3884.

[73] Z.C. Luo, M.X. Huang, Scr. Mater. 142 (2018) 28–31.